Supplemental Material: Ultra precise determination of Cs($nS_{1/2}$) and Cs(nD_J) quantum defects for sensing and computing: Evaluation of core contributions

Pinrui Shen,[1] Donald Booth,[1] Chang Liu,[1] Scott Beattie,[2] Claude Marceau,[2] James P. Shaffer,[1,*] Mariusz Pawlak,[3] and H. R. Sadeghpour[4,†]

[1] *Quantum Valley Ideas Laboratories, 485 Wes Graham Way, Waterloo, Ontario N2L 6R1, Canada*
[2] *National Research Council Canada, Ottawa, Ontario K1A 0R6, Canada*
[3] *Faculty of Chemistry, Nicolaus Copernicus University in Toruń, Gagarina 7, 87-100 Toruń, Poland*
[4] *ITAMP, Center for Astrophysics | Harvard & Smithsonian, 60 Garden St., Cambridge, Massachusetts 02138, USA*

(Dated: November 18, 2024)

I. HISTORICAL VALUE OF THE CS IONIZATION ENERGY

Historical measurements of the Cs ionization energy are summarized in Table S1. The improvements in the measurement uncertainty are illustrated in Fig. S1. The precision of the ionization energy has been improved over the past century.

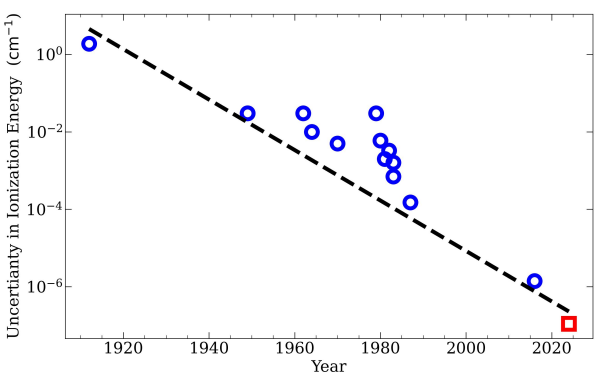

FIG. S1. Improvements in determining the ionization energy of the Cs atom over the last century. The uncertainties are reported in Refs. [1–14]. The red square represents the value reported in this work.

TABLE S1. The Cs ionization limit in cm^{-1} over the years.

Ref.	year	IE (cm^{-1})
Bevan [1]	1912	31 404.6(1.9)
Kratz [2]	1949	31 406.54(3)
McNally *et al.* [3]	1949	31 406.32(3)
Kleiman [4]	1962	31 406.450(30)
Bockasten [5]	1964	31 406.432(10)
Eriksson and Wenåker [6]	1970	31 406.454(5)
Lorenzen and Niemax [7]	1979	31 406.46(3)
Lorenzen *et al.* [8]	1980	31 406.468(6)
Sansonetti *et al.* [9]	1981	31 406.455 6(20)
Goy *et al.* [10]	1982	31 406.467 6(33)
O'Sullivan and Stoicheff [11]	1983	31 406.637 6(16)
Lorenzen and Niemax [12]	1983	31 406.471 0(7)
Weber and Sansonetti [13]	1987	31 406.467 66(15)
Deiglmayr *et al.* [14]	2016	31 406.467 732 5(14)
This work	2024	31 406.467 751 48(14)

II. ABSOLUTE FREQUENCY FITTING METHOD

Absolute frequency measurements are performed for the $nD_{5/2}, nD_{3/2}$, and $nS_{1/2}$ series. For the $nD_{3/2}$ and $nD_{5/2}$ series, the spectrum is fit to a multi-line Gaussian function,

$$f(\nu) = \sum_F (2F+1) \exp\left[-\frac{(\nu - \nu_F - \nu_0)^2}{2\sigma^2}\right], \quad (1)$$

which includes all possible hyperfine transitions weighted by the statistical factor of $(2F+1)$. F represents the total atomic angular momentum. For the $6S_{1/2} \to nD_{3/2}$ transitions, the possible hyperfine quantum numbers are $F = 2$ and 3. For the $6S_{1/2} \to nD_{5/2}$ transitions, F can be 1, 2, or 3. σ is the linewidth of the spectral line, assumed to be equal for all of the hyperfine transitions, since the dominant broadening mechanism is Doppler broadening. ν_0 in Eq. (1) is the frequency of the transitions from $|6S_{1/2}, F = 3\rangle$ to the center of gravity of the target Rydberg state, and ν_F is the hyperfine frequency shift from the center of gravity frequency. The value of ν_F can be calculated by [15, 16]

* e-mail: jshaffer@qvil.ca
† e-mail: hrs@cfa.harvard.edu

$$\nu_F = \frac{A^*_{\rm hfs}(n)}{2}K + B^*_{\rm hfs}(n)\frac{\frac{3}{2}K(K+1) - 2I(I+1)J(J+1)}{4I(2I-1)J(2J-1)} + C^*_{\rm hfs}(n)\frac{5K^2(K/4+1) + K[I(I+1)+J(J+1)+3-3I(I+1)J(J+1)] - 5I(I+1)J(J+1)}{I(I-1)(2I-1)J(J-1)(2J-1)}, \quad (2)$$

where

$$K = F(F+1) - I(I+1) - J(J+1). \quad (3)$$

Here, n is the principal quantum number, l is the orbital angular momentum quantum number, J is the total electron angular momentum quantum number, and I is the nuclear spin quantum number. $A^*_{\rm hfs}(n) = A_{\rm hfs}/[n-\delta^{(l,J)}]^3$, $B^*_{\rm hfs}(n) = B_{\rm hfs}/[n-\delta^{(l,J)}]^3$, and $C^*_{\rm hfs}(n) = C_{\rm hfs}/[n-\delta^{(l,J)}]^3$ are the reduced magnetic dipole, the electric quadruple, and the magnetic octupole hyperfine coupling constants, respectively, where $\delta^{(l,J)}$ is the quantum defect. Rahaman *et al.* [17] performed hyperfine structure measurements for the $7D_J$ states with the quantum interference corrections and reported $A^*_{\rm hfs}(7) = -1.7110(3)$ MHz, $B^*_{\rm hfs}(7) = -0.027(7)$ MHz, and $C^*_{\rm hfs}(7) = -0.02(80)$ kHz for the $7D_{5/2}$ state and $A^*_{\rm hfs}(7) = 7.3547(8)$ MHz, $B^*_{\rm hfs}(7) = -0.017(7)$ MHz, and $C^*_{\rm hfs}(7) = -0.3(4)$ kHz for the $7D_{3/2}$ state. Here, we also analyze the effect of the quantum interference (QI) on the measured Rydberg spectra. In our case, the Rydberg states are detected through ionization and counted by the MCP plate. We use pulse field ionization using a fast risetime pulse applied immediately after optical excitation. The atoms are ionized before any substantial spontaneous decay of the excited Rydberg atoms occurs. To experimentally verify that the effect is minimal in our experiment, we measured the $21D_{5/2}$ spectra at different polarization angles of the second excitation step laser ($\sim$ 509 nm) relative to the first excitation step laser ($\sim$ 852 nm). The fit of the $21D_{5/2}$ state center frequency is plotted as a function of the polarization angle in Fig. S2. The variation in the frequency of the center of the line shape representing the energy of the Rydberg state, obtained from the fit, is < 20 kHz and is constant within the uncertainty of the experiment. We conclude from the experiment that we can safely ignore the QI effect in our experiment.

For lower n, Eq. (1) is used to extract the center of gravity frequency of the transition. An example of a measured spectrum for $6S_{1/2} \rightarrow 28D_{3/2}$ is shown as Fig. S3(a). As n increases, the hyperfine frequency shift becomes smaller compared to the linewidth. A single Gaussian fitting function is used to extract the center frequency for $n > 60$, where the hyperfine splitting is calculated to be less than 10 kHz. The hyperfine frequency shift is calculated using Eq. (2) and used to correct the center frequency obtained from the Gaussian fit. The uncertainty in the hyperfine constant is also considered and taken as a source of uncertainty. For the $nS_{1/2}$ series, Eq. (1) is reduced to a single Gaussian function without

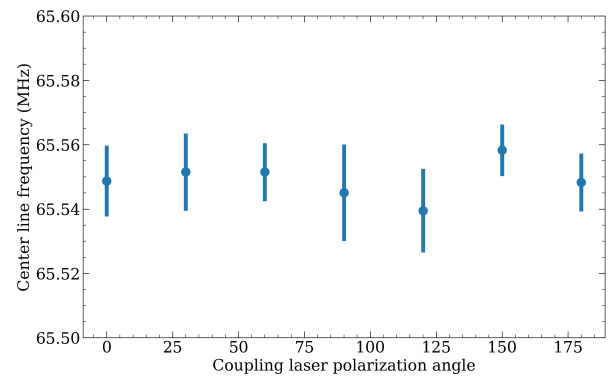

FIG. S2. Spectral line center versus the coupling laser ($\sim$ 509 nm) polarization angle relative to the $\sim$ 852 nm laser.

the statistical factor,

$$f(\nu) = \exp\left[-\frac{(\nu-\nu_F-\nu_0)^2}{2\sigma^2}\right], \quad (4)$$

as there is only one possible hyperfine transition, $|6S_{1/2}, F=3\rangle \rightarrow |nS_{1/2}, F'=3\rangle$. The magnetic dipole constant $A_{\rm hfs}$ for the $nS_{1/2}$ series is 13.53(12) GHz [18] and the electric quadruple constant, $B_{\rm hfs}$, and the magnetic octupole constant, $C_{\rm hfs}$, are zero. Similar to the corrections applied for nD_J series, the hyperfine splitting of the $nS_{1/2}$ series is also estimated and corrected. An example of a measured spectrum for $6S_{1/2} \rightarrow 80S_{1/2}$ is shown in Fig. S3(b). The summary of absolute frequency measurements for all three Cs series ($nS_{1/2}, nD_{3/2}$, and $nD_{5/2}$) are presented in Table S4.

III. UNCERTAINTY ANALYSIS

In Table S4, the statistical uncertainty is given in the bracket. The dominant source contributing to the statistical uncertainty is the shot-to-shot variation in the Rydberg ion counts. The uncertainty in the number of ions is measured to be $< 10\%$ and contributes less than 10 kHz to the total statistical uncertainty.

The uncertainty caused by the ion count fluctuations increases as the spectral linewidth broadens. Therefore, efforts were made to narrow the spectral linewidth. The dominant source of line broadening is the Doppler effect. To mitigate Doppler broadening, a polarization gradient cooling (PGC) step is used and optimized to cool the atoms to < 10 μK. With the orthogonal ex-

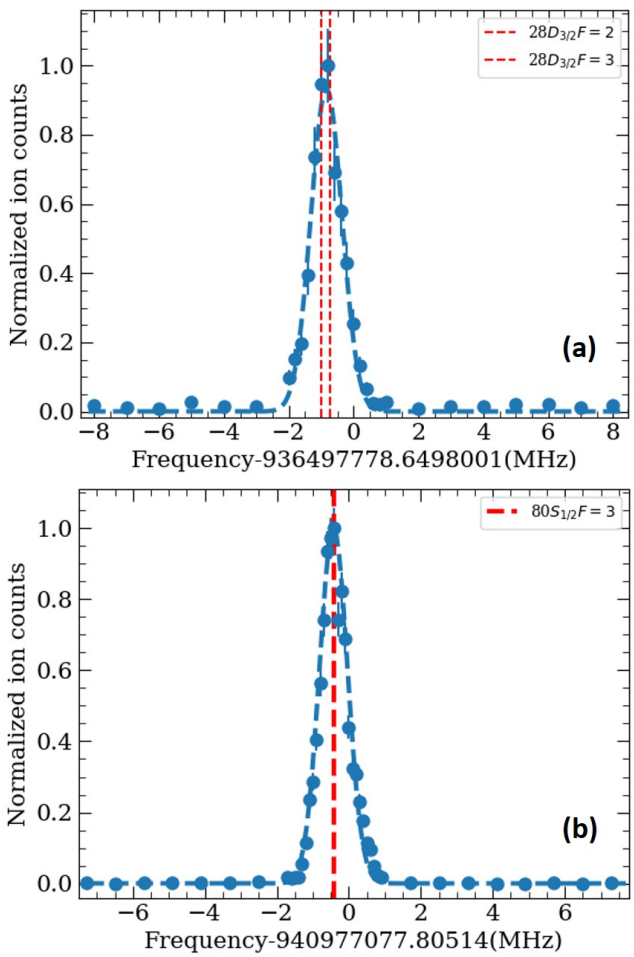

FIG. S3. Panel (a) shows an example of a measured spectrum for $6S_{1/2} \rightarrow 28D_{3/2}$. The spectrum is fit to a multi-line Gaussian function and yields a linewidth of 220 kHz. The corresponding hyperfine transitions are indicated by the red dashed lines. The lineshape is Gaussian because the dominant broadening mechanism is Doppler broadening. Panel (b) shows the spectrum for $6S_{1/2} \rightarrow 80S_{1/2}$, which is fit to a single Gaussian function (see text).

citation laser geometry, the Doppler broadening is estimated to be on the order of 200 kHz, which is close to the linewidth observed in the experiments, ≈ 250 kHz. Other possible contributions to the observed spectral linewidth are radiative decay of the intermediate $6P_{3/2}$ state and power broadening. The radiative decay rate is reduced to < 10 kHz by detuning the first-step laser 90 MHz away from the $6P_{3/2}$ resonance to adiabatically eliminate the intermediate state. The power broadening is suppressed to < 30 kHz by setting both excitation lasers' intensities below their respective saturation intensities. Pressure broadening and transit broadening are estimated to be on the order of 100 Hz, and thus negligible.

An additional contribution to the uncertainty is the determination of the laser frequency. The two excitation lasers are both locked to a GPS steered Rb clock frequency comb which has a stability of of 1.2×10^{-12} for a 10 s averaging time. However, the two lasers pass through AOMs before reaching the atoms. The RF signals driving the AOMs are derived from a quartz oscillator with a stability of 25 ppm. Taking into account the laser locking and the frequency shifts by the AOMs, the uncertainty in the laser frequency is < 2 kHz.

AC Stark shifts induced by the excitation laser fields are another source of uncertainty. Because the experiment was performed after the atoms are released from the molasses, there is no AC Stark shift from the trapping fields. The AC Stark shift induced by the ~ 509 nm laser is calculated to be negligible. Only the AC Stark shift on the ground state, $6S_{1/2}$, induced by the $\sim$ 852 nm laser needs to be considered. To characterize this shift, we measured a series of $54S_{1/2}$ spectra at different first-step laser powers. The measured center frequencies are plotted as a function of the $\sim$ 852 nm laser power, Fig. S4. The slope is found to be (0.45 ± 0.06) kHz/μW. For the experiments where we measured the Rydberg state spectra, the power of the $\sim$ 852 nm laser was set to 80.0 μW, which results a (36.0 ± 4.8) kHz blue AC Stark shift. Given that the beam waist and power level of the $\sim$ 852 nm laser are the same for all measurements, the AC Stark shift is applied as a shift for all Rydberg states. The shift has been applied to the values presented in Table S4 to correct the energy levels for a field-free environment. The uncertainty of the AC Stark shift, ± 4.8 kHz, is taken as a contribution to the uncertainty in determining the resonance frequency, listed in Table S2.

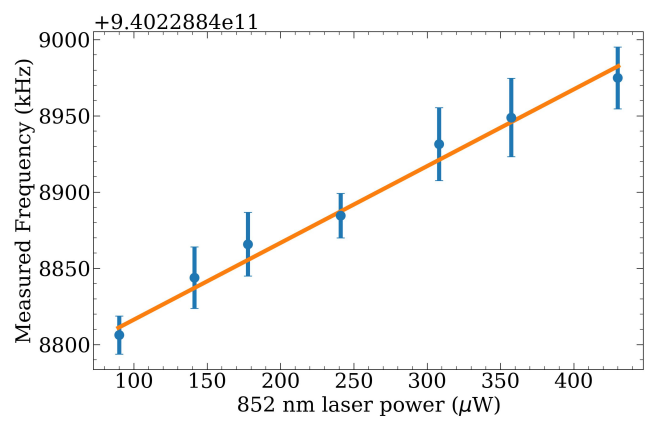

FIG. S4. AC Stark shift measurement. The absolute frequency of the $6S_{1/2} \rightarrow 54S_{1/2}$ transition is measured at different first-step laser power levels. Each data point is an average of five separate measurements and the error bar indicates the uncertainty of each data point derived from the average over the five measurements. The data is fit to a linear function (orange line), yielding a slope of (0.45 ± 0.06) kHz/μW.

Stray magnetic fields cause Zeeman shifts of the transitions. Compensation of the background magnetic field is required to obtain accurate spectroscopic measurements. The decay time of the eddy currents in the system as the MOT coils are shutdown is around 12 ms. To increase

TABLE S2. Uncertainties in the determination of the absolute frequency. The amplitude of each uncertainty is listed as the maximum possible value for any states measured in this work.

Sources	Amplitude (kHz)
Ground state AC Stark shift	$<$ 5.0
Zeeman effect shift	$<$ 14.3
DC Stark shift	$<$ 49.0
Hyperfine splitting	$<$ 4.0
Pressure shift	$<$ 2.8
Statistical uncertianty	$<$ 28.0
Total	$<$ 59.0

the decay rate of the eddy currents, we flipped the direction of the current in the MOT coils before extinguishing the magnetic field [19]. Using this approach, the decay time was shortened to less than 2.5 ms. Consequently, a wait time of 3 ms is added between the excitation stage and the extinction of the magnetic fields to reduce the magnetic fields from the eddy current. The other sources of the stray magnetic field are compensated using three pairs of Helmholtz coils placed around the MOT chamber. Microwave (MW) spectroscopy is used to determine the experimental amplitude of the total remaining magnetic field during the atom interrogation period. A similar method was used in Ref. [18] to compensate magnetic fields. The background magnetic field strength is reduced to $<$ 2 mG during the measurement of the Rydberg state transition frequencies, which results in a maximum Zeeman splitting of around 14.3 kHz. The sensitivity to the magnetic field is similar across all Rydberg states because they have the same Landé g-factor. The maximum Zeeman splitting, 14.3 kHz, is treated as a common error for all Rydberg states.

DC Stark effects can cause asymmetric line broadening, as well as a frequency shift. Stray electric fields need to be compensated in order to minimize the DC Stark shift. The stray electric fields are compensated using eight electrodes around the trapped atoms. We use the $160S_{1/2}$ state as a calibration state to minimize the Stark shifts. After carefully adjusting the voltage on each electrode, the electric field is reduced to $<$ 1 mV/cm. For the nD_J series, the DC Stark effect predominately causes broadening of the spectral linewidth. Based on the polarizability of Cs nD_J Rydberg states [20], the DC Stark effect introduces uncertainty that is no greater than 49 kHz for $90D_{5/2}$, while for $n = 27$, the systematic uncertainty induced by the stray electric field is no larger than 30 Hz. For the $nS_{1/2}$ series, the stray electric field primarily induces a frequency shift instead of line broadening. Due to the small polarizability of the Cs $nS_{1/2}$ states [21], the maximum DC stark effect induced frequency shift is no greater than 1.5 kHz for $90S_{1/2}$.

The pressure shift due to collisions between the Rydberg atoms and the surrounding ground state atoms is a source of uncertainty. Using the triplet s-wave e^-–Cs scattering length of $-22.7\ a_0$ [22] and the peak Cs cloud density of 2×10^{10} cm^{-3}, the maximum pressure shift is estimated to be $<$ 2.8 kHz for $n = 90$.

The main sources of the uncertainties are summarized in Table S2. For the low n states, the hyperfine splitting ($<$ 4.0 kHz) and the Zeeman splitting ($<$ 14.3 kHz) are the key uncertainties, while for the high n states, the DC Stark shift becomes dominant ($<$ 49.0 kHz). The dominant source contributing to the statistical uncertainty is the shot-to-shot variation of the ion counts. The median statistical uncertainty is $<$ 4.0 kHz, and the maximum statistical uncertainty is around 27.4 kHz due to one poor quality measurement.

IV. DISCUSSION OF THE ODD POWER TERMS IN MODIFIED RITZ FORMULA

According to Ref. [23], additional odd power terms should be considered in modified Ritz equation if core polarization makes a significant contribution to the energies, because the odd power terms result from second-order dipole polarization. We fit the nD_J series energy levels to modified Ritz equation with and without the odd power terms and compared the fit parameters. There are no significant changes to the values of the even quantum defects when including the odd power terms in the modified Ritz expansion. The contribution from the odd power terms is less than 0.01%. The quantum defects agree with an estimate of the core-polarization and core-penetration effects in Table II in the main text. We conclude that modified Ritz equation with only even power terms is suitable for accurately describing the energy levels of the Cs $nS_{1/2}, nP_J$, and nD_J states.

V. HIGHER ORDER ($k > 2$) QUANTUM DEFECT PARAMETERS

In this work, we report the quantum defect terms $\delta_{2k,k=0,1,2}$ up to the third order and found the higher order terms ($k > 2$) reported in previous work [12, 13] were negligible within the measurement uncertainties.

Here, we compare our reported quantum defects and prior quantum defects [13] against the observed $nS_{1/2}$ ($n = 8-90$) and $nD_{5/2}$ ($n = 8-90$) energies. The experimental data includes the measurements from Ref. [13] and the measurements in this work. We calculate the deviations characterized by the experimental uncertainty between the data and theoretical calculations using different sets of the quantum defects, as shown in Fig. S5. We find that the prior quantum defects with nonzero $k > 2$ values, obtained by fitting to observed energies for low-n Rydberg levels, do not reproduce our measurements for higher-n levels within uncertainty. However, the quantum defect parameters reported in this work, for high-n levels with zero $k > 2$

terms *reproduce* the previous observed levels at low n, as described in the main text.

It is possible that the lower n states are more sensitive to the higher order terms, but more precise measurements are required to extract their values. Our measurements show that the higher order $k > 2$ terms are not necessary to reproduce all the available data, including the low n states, within the experimental uncertainty for all of the measurements.

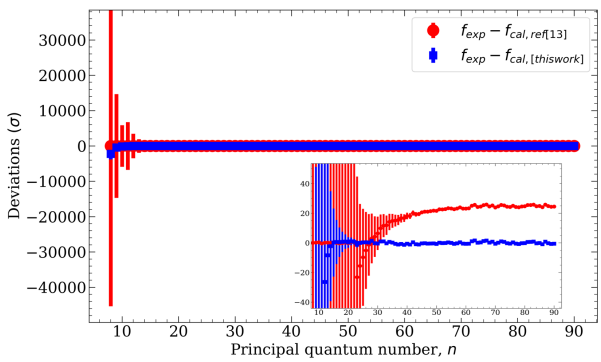

FIG. S5. Deviations between the experimental data and the energy level calculations. The experimental data consist of $nS_{1/2}$ ($n = 8$–27) measurements in Ref. [13] and $nS_{1/2}$ ($n = 28$–90) measurements in this work. Red circles represent the deviations in terms of the experimental uncertainty between the experimental data and the calculated energy levels based on the $nS_{1/2}$ quantum defects in Ref. [13]. Blue squares represent the deviations between the experimental data and the calculated energy levels based on the $nS_{1/2}$ quantum defects in this work. The error bars are the theoretical calculation uncertainties generated from the uncertainties in the quantum defects.

VI. ANALYTICAL FORM OF THE EXPECTATION VALUE OF THE SPIN–ORBIT COUPLING FOR HYDROGENIC WAVE FUNCTIONS

We show that the dominant term of the expectation value of spin–orbit coupling for hydrogenic wave functions scales in proportion to n^{-3}, and the next two as n^{-5} and n^{-7}, assuming the atomic potential to be a Coulomb potential with spherically symmetric core polarization.

The spin-orbit interaction potential is usually given by

$$V^{\rm LS}(r) = \frac{1}{2\mu^2 c^2}\left(\frac{1}{r}\frac{{\rm d}V}{{\rm d}r}\right)\mathbf{L}\cdot\mathbf{S}, \tag{5}$$

where μ is the reduced mass and c is the speed of light. As an attractive potential, we take the Coulomb potential with nuclear charge Ze in conjunction with the core polarization term,

$$V(r) = -\frac{1}{4\pi\varepsilon_0}\frac{Ze^2}{r} - \left(\frac{e}{4\pi\varepsilon_0}\right)^2\frac{\alpha_c}{2r^4}, \tag{6}$$

where α_c is static dipole polarizability of the core. The derivative of $V(r)$ divided by r is

$$\frac{1}{r}\frac{{\rm d}V(r)}{{\rm d}r} = \frac{Ze^2}{4\pi\varepsilon_0}\frac{1}{r^3} + \left(\frac{e}{4\pi\varepsilon_0}\right)^2\frac{2\alpha_c}{r^6}. \tag{7}$$

Acting from both sides with a hydrogenic wave function, we obtain

$$\left\langle\frac{1}{r}\frac{{\rm d}V}{{\rm d}r}\right\rangle_{n,l} = \frac{Ze^2}{4\pi\varepsilon_0}\left\langle\frac{1}{r^3}\right\rangle_{n,l} + \left(\frac{e}{4\pi\varepsilon_0}\right)^2 2\alpha_c\left\langle\frac{1}{r^6}\right\rangle_{n,l}, \tag{8}$$

where

$$\left\langle\frac{1}{r^3}\right\rangle_{n,l} = \frac{Z^3}{a_\mu^3(l+\frac{1}{2})l(l+1)}\frac{1}{n^3}, \tag{9}$$

$$\left\langle\frac{1}{r^6}\right\rangle_{n,l} = \frac{Z^6}{D}\left(A\frac{1}{n^3} + B\frac{1}{n^5} + C\frac{1}{n^7}\right), \tag{10}$$

$$A = 140, \tag{11}$$

$$B = 20[5 - 6l(l+1)], \tag{12}$$

$$C = 12l(l^2-1)(l+2), \tag{13}$$

$$D = a_\mu^6 l(l+1)(2l+1)[l(l+1)-2] \times[4l(l+1)-15][4l(l+1)-3], \tag{14}$$

and a_μ is the reduced Bohr radius, $a_\mu = \frac{m_e}{\mu}a_0$. Note that Eq. (9) holds for $l > 0$, whereas Eq. (10) for $l > 1$. The effect of the $\mathbf{L}\cdot\mathbf{S}$ term in respect of the l, s, J, m_J quantum numbers is as follows

$$\langle\mathbf{L}\cdot\mathbf{S}\rangle^{(l,J)} = \frac{\hbar^2}{2}\left[J(J+1) - l(l+1) - \frac{3}{4}\right]. \tag{15}$$

The fine-structure splitting can be obtained as $\Delta_{\rm fs} \approx \langle V^{\rm LS}\rangle_{n,l,J>l} - \langle V^{\rm LS}\rangle_{n,l,J<l}$, where the dominant terms are proportional to n^{-3}, n^{-5}, and n^{-7}, respectively. This justifies the form of the fine-structure splitting expansion,

$$\Delta_{\rm fs} = \sum_{q=1}^{\infty}\frac{\xi_q^{(l)}}{[n - \tilde{\delta}^{(l,J=l\pm1)}(n)]^{2q+1}}. \tag{16}$$

The weighted average quantum defect, $\tilde{\delta}^{(l,J=l\pm1)}(n) = w^{(l,J<l)}\delta^{(l,J<l)}(n) + w^{(l,J>l)}\delta^{(l,J>l)}(n)$, comprises the quantum defects weighted by the $\mathbf{L}\cdot\mathbf{S}$ term; $w^{(l,J)} = 1 - \frac{|\langle\mathbf{L}\cdot\mathbf{S}\rangle^{(l,J)}|}{\hbar^2(l+1/2)}$.

VII. NUMERICAL CALCULATIONS OF WAVE FUNCTIONS AND REDUCED ELECTRIC-DIPOLE MATRIX ELEMENTS

The Hamiltonian describing the valence electron in the field of an alkali-metal positive-ion core reads (in a.u.)

$$\hat{H} = -\frac{1}{2\mu}\nabla^2 + V_l(r) + V_l^{\rm LS}(r), \tag{17}$$

where μ is the reduced mass, $V_l(r)$ is the model interaction potential [24], and $V_l^{\rm LS}(r)$ is the spin–orbit coupling [25]. The l-dependent effective potential, $V_l(r)$, including a polarization term is (in a.u.)

$$V_l(r) = -\frac{1+(Z-1)\exp\left[-a_1^{(l)}r\right]}{r} + \left(a_3^{(l)} + a_4^{(l)}r\right)\exp\left[-a_2^{(l)}r\right] - \frac{\alpha_c}{2r^4}\left(1-\exp\left[-\left(r/r_c^{(l)}\right)^6\right]\right), \quad (18)$$

where Z is the nuclear charge number and α_c is the static dipole polarizability. Five parameters ($r_c^{(l)}$, $a_1^{(l)}$, $a_2^{(l)}$, $a_3^{(l)}$, and $a_4^{(l)}$) are given for different alkali-metal atoms in Ref. [24]. The next term in the Hamiltonian, describing the spin–orbit interaction, could be expressed in the non-trivial form (in a.u.) [25]

$$V_l^{\rm LS}(r) = \frac{1}{2\mu^2c^2}\left(\frac{1}{r}\frac{{\rm d}V_l(r)}{{\rm d}r}\right)\mathbf{L}\cdot\mathbf{S}\left(1-\frac{1}{2\mu^2c^2}V_l(r)\right)^{-2}. \quad (19)$$

The last part of $V_l^{\rm LS}$ guarantees proper behavior of wave functions at short range.

We calculated the wave functions of the time-independent Schrödinger equation by numerical integration utilizing Numerov's method with energies determined from our quantum defects. We set the integration interval as $[0.01, 2n(n+15)]$ (in a.u.), divided into 4×10^6 equal segments. All obtained functions have attained the appropriate behavior close to the origin as well as asymptotic behavior. We calculated (within composite Simpson's rule) the expectation values of r, $V_l^{\rm LS}$, and each term of V_l. Subsequently, we estimated the numerical $\Delta_{\rm fs}$ for the nD_J series by $\langle V_{l=2}^{\rm LS}\rangle_{n,l=2,J=5/2} - \langle V_{l=2}^{\rm LS}\rangle_{n,l=2,J=3/2}$.

The model potential is viewed as a combination interaction of core penetration and core polarization. The first two terms in Eq. (18) are usually considered as the core penetration dominant term, $V_{\rm pen}(r)$, while the third term is the result of core polarization, $V_{\rm pol}(r)$. Then, the energy contributions from core polarization and core penetration are $\langle V_{\rm pol}\rangle$ and $\langle V_{\rm pen}\rangle$, respectively.

Moreover, based on our results and quantum defects for the nP_J states from Ref. [14], we determined the reduced electric-dipole matrix elements for $n'P_{J'} \leftrightarrow nD_J$ transitions according to

$$\langle J'||r||J\rangle = (-1)^{l+J+s'+1}\sqrt{(2J'+1)(2J+1)}\delta_{s',s} \times \begin{Bmatrix} l' & J' & s' \\ J & l & 1 \end{Bmatrix}\langle l'||r||l\rangle, \quad (20)$$

where

$$\langle l'||r||l\rangle = (-1)^{l'}\sqrt{(2l'+1)(2l+1)} \times \begin{pmatrix} l' & 1 & l \\ 0 & 0 & 0 \end{pmatrix}\langle n'l'J'|r|nlJ\rangle. \quad (21)$$

The results for low-lying states are compared with the computed values of Safronova *et al.* [26] and for highly excited states with the results from ARC [27], see Table S3.

TABLE S3. The reduced electric-dipole matrix elements (in a.u.).

Transition	Other works	This work
$7D_{3/2} \leftrightarrow 7P_{1/2}$	6.6(2) [26]	6.5814
$7D_{3/2} \leftrightarrow 8P_{1/2}$	32.0(1) [26]	31.9943
$7D_{3/2} \leftrightarrow 9P_{1/2}$	9.0(2) [26]	8.8867
$7D_{3/2} \leftrightarrow 10P_{1/2}$	2.86(8) [26]	2.8524
$7D_{3/2} \leftrightarrow 11P_{1/2}$	1.55(4) [26]	1.5506
$7D_{3/2} \leftrightarrow 12P_{1/2}$	1.03(3) [26]	1.0268
$7D_{3/2} \leftrightarrow 7P_{3/2}$	3.3(1) [26]	3.3328
$7D_{3/2} \leftrightarrow 8P_{3/2}$	14.35(5) [26]	14.3587
$7D_{3/2} \leftrightarrow 9P_{3/2}$	3.56(9) [26]	3.5040
$7D_{3/2} \leftrightarrow 10P_{3/2}$	1.16(4) [26]	1.1603
$7D_{3/2} \leftrightarrow 11P_{3/2}$	0.64(2) [26]	0.6354
$7D_{3/2} \leftrightarrow 12P_{3/2}$	0.42(1) [26]	0.4219
$7D_{5/2} \leftrightarrow 7P_{3/2}$	9.6(3) [26]	9.6960
$7D_{5/2} \leftrightarrow 8P_{3/2}$	43.2(1) [26]	43.2245
$7D_{5/2} \leftrightarrow 9P_{3/2}$	11.1(2) [26]	10.9461
$7D_{5/2} \leftrightarrow 10P_{3/2}$	3.6(1) [26]	3.5939
$7D_{5/2} \leftrightarrow 11P_{3/2}$	1.97(6) [26]	1.9640
$7D_{5/2} \leftrightarrow 12P_{3/2}$	1.31(4) [26]	1.3030
$8D_{3/2} \leftrightarrow 9P_{1/2}$	49.3(1) [26]	49.2834
$8D_{3/2} \leftrightarrow 9P_{3/2}$	22.14(7) [26]	22.1317
$8D_{5/2} \leftrightarrow 9P_{3/2}$	66.6(2) [26]	66.5588
$9D_{3/2} \leftrightarrow 10P_{1/2}$	70.0(1) [26]	69.9676
$9D_{3/2} \leftrightarrow 10P_{3/2}$	31.45(8) [26]	31.4347
$9D_{5/2} \leftrightarrow 10P_{3/2}$	94.5(2) [26]	94.4738
$10D_{3/2} \leftrightarrow 11P_{1/2}$	94.1(2) [26]	94.0566
$10D_{3/2} \leftrightarrow 11P_{3/2}$	42.29(9) [26]	42.2721
$10D_{5/2} \leftrightarrow 11P_{3/2}$	127.0(2) [26]	126.9827
$11D_{3/2} \leftrightarrow 12P_{1/2}$	121.6(2) [26]	121.5538
$11D_{3/2} \leftrightarrow 12P_{3/2}$	54.66(9) [26]	54.6452
$11D_{5/2} \leftrightarrow 12P_{3/2}$	164.1(2) [26]	164.0899
$30D_{3/2} \leftrightarrow 30P_{1/2}$	164.5663 [27]	164.5625
$30D_{3/2} \leftrightarrow 30P_{3/2}$	89.8979 [27]	89.8519
$30D_{5/2} \leftrightarrow 30P_{3/2}$	255.9199 [27]	255.7829
$40D_{3/2} \leftrightarrow 40P_{1/2}$	297.6955 [27]	297.6939
$40D_{3/2} \leftrightarrow 40P_{3/2}$	163.4144 [27]	163.3215
$40D_{5/2} \leftrightarrow 40P_{3/2}$	464.5782 [27]	464.2992
$50D_{3/2} \leftrightarrow 50P_{1/2}$	469.9097 [27]	469.9095
$50D_{3/2} \leftrightarrow 50P_{3/2}$	258.6886 [27]	258.5334
$50D_{5/2} \leftrightarrow 50P_{3/2}$	734.8516 [27]	734.3844
$60D_{3/2} \leftrightarrow 60P_{1/2}$	681.2107 [27]	681.2114
$60D_{3/2} \leftrightarrow 60P_{3/2}$	375.7211 [27]	375.4885
$60D_{5/2} \leftrightarrow 60P_{3/2}$	1066.7426 [27]	1066.0418
$70D_{3/2} \leftrightarrow 70P_{1/2}$	931.5993 [27]	931.6004
$70D_{3/2} \leftrightarrow 70P_{3/2}$	514.5122 [27]	514.1874
$70D_{5/2} \leftrightarrow 70P_{3/2}$	1460.2520 [27]	1459.2724
$80D_{3/2} \leftrightarrow 80P_{1/2}$	1221.0759 [27]	1221.0769
$80D_{3/2} \leftrightarrow 80P_{3/2}$	675.0622 [27]	674.6302
$80D_{5/2} \leftrightarrow 80P_{3/2}$	1915.3803 [27]	1914.0768

TABLE S4. Absolute frequency measurements and the statistical uncertainties of transitions from the $|6S_{1/2}, F = 3\rangle$ hyperfine ground state to the center of gravity of the $nS_{1/2}$, $nD_{5/2}$, $nD_{3/2}$ states. The statistical uncertainties are presented in the brackets.

n	$\nu_{S_{1/2}}$(kHz)	$\nu_{D_{5/2}}$(kHz)	$\nu_{D_{3/2}}$(kHz)
21	—	931969904159.4(6.2)	931960462840.3(16.9)
22	—	932925420315.1(9.9)	932917355120.8(27.0)
23	932386112252.8(10.9)	933744762535.1(6.1)	933737818429.9(5.3)
24	933281572697.2(9.1)	934452628487.4(8.2)	934446607025.4(5.7)
25	934051877594.8(6.0)	935068360508.0(5.3)	935063105302.8(7.6)
26	934719309793.5(6.2)	935607280846.3(4.3)	935602667250.9(11.4)
27	935301404781.5(5.8)	936081653844.5(6.7)	936077581723.7(25.5)
28	935812114821.2(6.6)	936501390829.7(11.6)	936497778401.0(9.4)
29	936262652614.1(6.6)	936874570954.1(11.0)	936871351515.9(14.4)
30	936662113134.8(23.2)	937207833091.9(3.5)	937204951761.9(9.0)
31	937017935503.2(7.8)	937506674118.6(7.4)	937504085293.8(17.5)
32	937336251966.1(6.8)	937775676305.4(12.9)	937773341520.9(27.4)
33	937622154361.1(6.6)	938018683599.5(12.0)	938016570610.9(21.0)
34	937879899105.2(5.8)	938238940313.9(6.9)	938237022105.7(20.4)
35	938113065775.6(5.9)	938439200875.3(7.1)	938437453971.2(10.3)
36	938324682925.2(7.5)	938621813939.2(11.5)	938620218885.2(18.0)
37	938517326596.3(6.1)	938788794105.1(6.1)	938787333466.2(11.6)
38	938693199099.5(13.8)	938941875772.7(8.4)	938940534869.6(13.0)
39	938854192054.4(6.7)	939082559923.6(6.3)	939081326162.6(11.3)
40	939001938005.6(4.9)	939212149979.8(5.3)	939211012223.6(11.8)
41	939137851248.8(5.5)	939331782115.4(3.3)	939330730785.5(6.5)
42	939263162645.1(4.3)	939442451581.3(3.2)	939441477865.5(6.1)
43	939378946543.6(4.4)	939545031475.7(2.8)	939544128149.5(4.5)
44	939486145108.6(5.6)	939640291542.0(3.8)	939639452038.1(4.0)
45	939585586643.1(5.6)	939728912110.0(2.2)	939728130311.4(4.1)
46	939678001804.1(3.9)	939811496008.9(2.3)	939810766742.1(3.9)
47	939764037301.9(4.5)	939888579281.8(4.5)	939887898202.6(4.5)
48	939844267171.4(3.3)	939960639986.8(3.9)	939960002633.6(6.9)
49	939919202219.9(4.1)	940028105046.6(2.7)	940027507933.1(5.2)
50	939989298297.8(3.1)	940091356980.5(2.3)	940090796847.7(6.3)
51	940054963356.3(3.7)	940150739757.1(3.0)	940150213503.5(4.0)
52	940116562993.4(3.2)	940206562229.9(3.3)	940206067286.4(5.1)
53	940174426104.1(3.2)	940259103796.2(3.9)	940258637730.8(4.0)
54	940228848894.2(3.3)	940308616656.9(2.8)	940308176949.6(4.0)
55	940280098714.1(2.8)	940355328595.1(2.5)	940354913714.3(3.4)
56	940328417535.4(2.6)	940399447726.2(2.7)	940399055410.9(4.0)
57	940374024757.6(2.6)	940441161862.7(2.7)	940440790798.0(3.7)
58	940417119508.6(2.8)	940480642898.3(3.0)	940480291683.7(3.7)
59	940457882873.4(2.7)	940518047613.3(2.9)	940517714586.4(4.0)
60	940496480189.1(2.9)	940553518755.5(2.8)	940553202814.9(3.7)
61	940533062211.7(3.9)	940587187563.1(2.9)	940586887573.7(4.0)
62	940567766937.4(2.6)	940619174003.0(2.9)	940618888798.3(4.0)
63	940600720478.7(2.8)	940649588356.1(3.1)	940649317128.1(4.6)
64	940632038624.7(2.5)	940678532080.7(3.3)	940678273721.2(6.8)
65	940661828075.4(2.9)	940706098240.3(3.0)	940705852154.6(3.6)
66	940690186672.2(2.4)	940732373107.7(2.8)	940732138396.3(3.5)
67	940717204520.9(2.7)	940757435910.2(2.9)	940757211965.9(3.4)
68	940742964737.3(2.8)	940781360273.0(3.3)	940781146543.5(4.9)
69	940767544436.6(2.9)	940804213858.0(3.3)	940804009611.6(4.3)
70	940791014390.2(2.6)	940826059993.4(2.9)	940825864543.3(4.0)
71	940813440688.8(2.9)	940846956605.6(3.2)	940846769709.6(5.1)
72	940834884192.3(3.2)	940866958354.9(2.9)	940866779386.3(4.3)
73	940855401394.3(3.0)	940886115318.8(3.1)	940885943816.9(4.5)
74	940875044929.6(3.0)	940904474457.7(3.0)	940904310172.5(3.9)
75	940893863785.4(2.6)	940922079455.2(3.8)	940921921920.8(4.3)
76	940911903524.6(2.5)	940938971360.0(3.5)	940938819935.9(4.9)
77	940929206377.2(3.4)	940955187877.3(3.0)	940955042412.3(4.1)
78	940945812091.5(4.2)	940970764457.6(2.8)	940970624780.2(5.0)
79	940961757637.3(2.8)	940985734322.3(3.1)	940985600177.7(4.7)
80	940977077468.5(3.0)	941000129023.3(2.8)	940999999914.6(5.0)
81	940991803979.2(3.1)	941013977102.4(3.3)	941013852909.6(4.1)
82	941005967315.5(3.3)	941027306402.3(2.8)	941027186804.4(4.4)
83	941019595894.5(3.0)	941040141871.0(3.0)	941040026757.3(4.0)
84	941032716195.4(3.3)	941052508233.8(3.6)	941052397262.3(6.7)
85	941045353362.2(2.8)	941064427739.9(3.8)	941064320777.0(4.3)
86	941057530672.1(4.0)	941075921921.6(2.9)	941075818628.5(3.8)
87	941069270411.2(3.2)	941087010435.1(3.6)	941086910744.6(3.9)
88	941080592943.8(3.0)	941097712195.3(3.0)	941097616114.7(5.5)
89	941091518016.1(3.5)	941108045350.2(4.5)	941107952468.8(6.4)
90	941102064029.3(3.1)	941118026228.4(4.7)	941117936446.0(7.2)

[1] P. V. Bevan, Spetroscopic observations: Lithium and cœsium, Proc. R. Soc. A **86**, 320 (1912).

[2] H. R. Kratz, The principal series of potassium, rubidium, and cesium in absorption, Phys. Rev. **75**, 1844 (1949).

[3] J. R. McNally, J. P. Molnar, W. J. Hitchcock, and N. F. Oliver, High members of the principal series in caesium, J. Opt. Soc. Am. **39**, 57 (1949).

[4] H. Kleiman, Interferometric measurements of cesium I, J. Opt. Soc. Am. **52**, 441 (1962).

[5] K. Bockasten, Polarization formula for the ^2F-series of CsI, J. Opt. Soc. Am. **54**, 1065 (1964).

[6] K. B. S. Eriksson and I. Wenåker, New wavelength measurements in Cs I, Phys. Scr. **1**, 21 (1970).

[7] C.-J. Lorenzen and K. Niemax, New measurements of the $n^2P_{1/2,3/2}$ energy levels of Cs(I), J. Quant. Spectrosc. Radiat. Transf. **22**, 247 (1979).

[8] C.-J. Lorenzen, K.-H. Weber, and K. Niemax, Energies of the $n^2S_{1/2}$ and $n^2D_{3/2,5/2}$ states of Cs, Opt. Commun. **33**, 271 (1980).

[9] C. J. Sansonetti, K. L. Andrew, and J. Verges, Polarization, penetration, and exchange effects in the hydrogen-like nf and ng terms of cesium, J. Opt. Soc. Am. **71**, 423 (1981).

[10] P. Goy, J. M. Raimond, G. Vitrant, and S. Haroche, Millimeter-wave spectroscopy in cesium Rydberg states. Quantum defects, fine- and hyperfine-structure measurements, Phys. Rev. A **26**, 2733 (1982).

[11] M. S. O'Sullivan and B. P. Stoicheff, Doppler-free two-photon absorption spectrum of cesium, Can. J. Phys. **61**, 940 (1983).

[12] C.-J. Lorenzen and K. Niemax, Non-monotonic variation of the quantum defect in Cs nD_J term series, Z. Phys. A **311**, 249 (1983).

[13] K.-H. Weber and C. J. Sansonetti, Accurate energies of nS, nP, nD, nF, and nG levels of neutral cesium, Phys. Rev. A **35**, 4650 (1987).

[14] J. Deiglmayr, H. Herburger, H. Saßmannshausen, P. Jansen, H. Schmutz, and F. Merkt, Precision measurement of the ionization energy of Cs I, Phys. Rev. A **93**, 013424 (2016).

[15] D. Steck, Cesium D line data, available online at `http://steck.us/alkalidata` (revision 2.0.1, 2 May 2008).

[16] V. Gerginov, A. Derevianko, and C. E. Tanner, Observation of the nuclear magnetic octupole moment of ^{133}Cs, Phys. Rev. Lett. **91**, 072501 (2003).

[17] B. Rahaman, S. C. Wright, and S. Dutta, Observation of quantum interference of optical transition pathways in Doppler-free two-photon spectroscopy and implications for precision measurements, Phys. Rev. A **109**, 042820 (2024).

[18] H. Saßmannshausen, F. Merkt, and J. Deiglmayr, High-resolution spectroscopy of Rydberg states in an ultracold cesium gas, Phys. Rev. A **87**, 032519 (2013).

[19] C. J. Dedman, K. G. H. Baldwin, and M. Colla, Fast switching of magnetic fields in a magneto-optic trap, Review of Scientific Instruments **72**, 4055 (2001).

[20] M. Auzinsh, K. Bluss, R. Ferber, F. Gahbauer, A. Jarmola, M. S. Safronova, U. I. Safronova, and M. Tamanis, Level-crossing spectroscopy of the 7, 9, and $10D_{5/2}$ states of ^{133}Cs and validation of relativistic many-body calculations of the polarizabilities and hyperfine constants, Phys. Rev. A **75**, 022502 (2007).

[21] J. Bai, S. Bai, X. Han, Y. Jiao, J. Zhao, and S. Jia, Precise measurements of polarizabilities of cesium nS Rydberg states in an ultra-cold atomic ensemble, New J. Phys. **22**, 093032 (2020).

[22] I. I. Fabrikant, Interaction of Rydberg atoms and thermal electrons with K, Rb and Cs atoms, J. Phys. B: At. Mol. Opt. Phys. **19**, 1527 (1986).

[23] G. W. F. Drake and R. A. Swainson, Quantum defects and the $1/n$ dependence of Rydberg energies: Second-order polarization effects, Phys. Rev. A **44**, 5448 (1991).

[24] M. Marinescu, H. R. Sadeghpour, and A. Dalgarno, Dispersion coefficients for alkali-metal dimers, Phys. Rev. A **49**, 982 (1994).

[25] M. Aymar, C. H. Greene, and E. Luc-Koenig, Multichannel Rydberg spectroscopy of complex atoms, Rev. Mod. Phys. **68**, 1015 (1996).

[26] M. S. Safronova, U. I. Safronova, and C. W. Clark, Magic wavelengths, matrix elements, polarizabilities, and lifetimes of Cs, Phys. Rev. A **94**, 012505 (2016).

[27] N. Šibalić, J. D. Pritchard, C. S. Adams, and K. J. Weatherill, ARC: An open-source library for calculating properties of alkali Rydberg atoms, Comput. Phys. Commun. **220**, 319 (2017).